Journal of Materials Chemistry A

ROYAL SOCIETY OF CHEMISTRY

PAPER

View Article Online
View Journal | View Issue

Cite this: J. Mater. Chem. A, 2024, 12, 17510

Effect of vanadium doping on α-K_xMnO_2 as a positive electrode active material for rechargeable magnesium batteries†

Isaac Oda-Bayliss,[a] Shunsuke Yagi, *[a] Masao Kamiko,[a] Kai Shimada,[a] Hiroaki Kobayashi [b] and Tetsu Ichitsubo [c]

Received 29th January 2024
Accepted 6th June 2024

DOI: 10.1039/d4ta00659c

rsc.li/materials-a

α-MnO_2 has recently attracted attention as a promising candidate for positive electrode active materials for rechargeable magnesium batteries (RMBs) due to its ability to accommodate Mg^{2+} ions without phase changes at limited concentrations. However, the stability of this phase and the kinetic barriers to Mg^{2+} insertion remain significant challenges. This study purposes doping of potassium stabilized hollandite MnO_2 (α-K_xMnO_2) with vanadium ions as a method to improve the stability and cyclability of the α-K_xMnO_2 phase. RMBs with V-doped α-K_xMnO_2 positive electrode active materials exhibit discharge potentials over 0.2 V greater than that of undoped α-K_xMnO_2, and improved magnesiation and demagnesiation upon discharge and charge, respectively. V-doped α-K_xMnO_2 also exhibits greater preference for reduction *via* Mg^{2+} insertion, compared to conversion to disparate phase oxides, enhancing the stability of the α-K_xMnO_2 phase, and increasing capacity retention upon battery cycling.

1 Introduction

Currently lithium-ion batteries (LIBs) are employed across a wide array of practical applications, due to their high energy density and rate capability. However, as the scale of applications increases, the need for further increases in energy density has become apparent. One major factor limiting the energy density of LIBs is the low theoretical specific capacity of the carbonaceous negative electrode active materials (372 mA h g^{-1}). While the use of a lithium metal negative electrode would result in a much greater capacity, the dendritic deposition of lithium metal upon charging and the associated short circuit risk make this substitution difficult.[1] As a result, in recent years increased attention has turned to alternative batteries using metallic negative electrodes such as Mg, Ca, and Al.

Among these candidates, one of the most promising is Mg; Mg metal has a high specific capacity (*ca.* 2200 mA h g^{-1}) and exhibits non-dendritic plating,[2–6] allowing for use as a safe battery negative electrode. Aurbach *et al.* pioneered the field of rechargeable magnesium batteries (RMBs) when they demonstrated Chevrel phase Mo_6S_8 as a positive electrode active material enabling reversible Mg insertion/extraction.[7] However, this Chevrel phase Mo_6S_8 exhibited both low discharge potential (1.1–1.2 V *vs.* Mg/Mg^{2+}) and capacity (~75 mA h g^{-1}). Therefore, subsequent research in the field of RMBs has focused on finding positive electrode active materials that improve these two key characteristics.

Due to the typically higher redox potentials of oxides compared to sulfides, significant efforts have been made to develop metal oxide positive electrode active materials with relatively high discharge potentials and capacities, such as olivine $MgCoSiO_4$ (~1.5 V *vs.* Mg/Mg^{2+}, 250 mA h g^{-1}),[8] spinel $MgMn_2O_4$ (~2.9 V *vs.* Mg/Mg^{2+}, 180 mA h g^{-1}),[9] $MgCo_2O_4$ (~2.9 V *vs.* Mg/Mg^{2+}, 200 mA h g^{-1}),[10] and $MgFe_2O_4$ (~2.5 V *vs.* Mg/Mg^{2+}, 110 mA h g^{-1}).[11,12]

While these spinel type oxides in particular possess high discharge potentials and initial capacities, they exhibit significant capacity degradation upon battery cycling, partly due to their conversion from the spinel to the rock-salt phase upon magnesiation.[10] The high electrostatic interaction between Mg^{2+} ions and the host framework, combined with the high stability of the rock-salt phase greatly limit Mg^{2+} extraction upon charge, decreasing cyclability.

To improve battery cyclability at higher potentials, we turned to hollandite manganese oxide (α-MnO_2) as a positive electrode active material for RMBs. α-MnO_2 is a polymorph of manganese oxide formed by conjoined MnO_6 octahedra and characterized by long 1D tunnels with side lengths of two octahedra. These 2 × 2 tunnels are often stabilized by a large cation located at the tunnel centre as shown in Fig. 1. One of the most common

[a]Institute of Industrial Science, The University of Tokyo, 4-6-1 Komaba, Meguro-ku, Tokyo 153-8505, Japan. E-mail: syagi@iis.u-tokyo.ac.jp
[b]Department of Chemistry, Faculty of Science, Hokkaido University, Kita 10, Nishi 8, Kita-ku, Sapporo, Hokkaido 060-0810, Japan
[c]Institute for Materials Research, Tohoku University, 2-1-1 Katahira, Aoba-ku, Sendai 980-8577, Japan

† Electronic supplementary information (ESI) available. See DOI: https://doi.org/10.1039/d4ta00659c

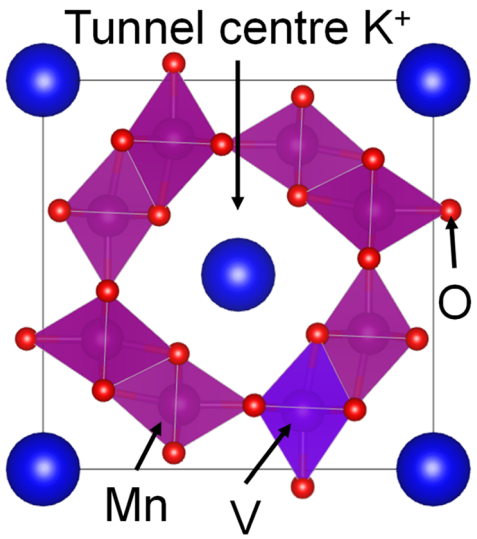

Fig. 1 Schematic diagram of potassium stabilized hollandite manganese oxide (α-K_xMnO_2) with K, Mn, O and substituted V positions labelled. VESTA 3 is used for three-dimensional visualization of the crystal.

forms of hollandite α-MnO_2 is cryptomelane (α-K_xMnO_2), in which K^+ ions occupy the tunnel centre sites.

α-MnO_2 has been extensively studied as a positive electrode active material in LIBs and was an early metal oxide candidate considered for use in RMBs.[13] However, Ling *et al.*[14] and Arthur *et al.*[15] showed that the primary mode of magnesiation of α-MnO_2 was not by Mg^{2+} insertion, but by surface Mg enrichment and conversion to Mg–O and Mn–O compounds due to the high stability of MgO.

$$MnO_2 + yMg^{2+} + 2ye^- \rightarrow yMgO + MnO_{2-y},$$

This irreversible reaction mechanism was thought to limit the utility of α-MnO_2 as a positive electrode active material for RMBs.

However, Hatakeyama *et al.* recently showed at elevated temperatures (150 °C) that α-MnO_2 could exhibit insertion and extraction of Mg^{2+} up to 220 mA h g^{-1} with an initial discharge potential of 2.6 V *vs.* Mg/Mg^{2+} without phase transformation.[16]

$$MnO_2 + yMg^{2+} + 2ye^- \leftrightarrow Mg_yMnO_2,$$

While these findings elucidated the role of reaction kinetics in the magnesiation pathway, there were still several limitations to the application of α-MnO_2 as a positive electrode active material for RMBs. Namely, the high electrostatic interaction of Mg^{2+} ions and the α-MnO_2 host framework resulted in magnesium buildup upon cycling and capacity degradation, indicating the need for further decrease in kinetic barriers.

To minimize the kinetic barriers to magnesiation, we looked to two potential methods by which α-MnO_2 can be modified that have been shown to improve battery performance in LIBs.

These methods were partial substitution of framework Mn with disparate transition metal ions,[17–21] and modification of the concentration and species of the tunnel centre cations.[22–24]

Of particular interest for the motivation of this work were two previous studies. First, Poyraz *et al.* examined the effect of tunnel centre K^+ concentration in the α-K_xMnO_2 electrode on LIB performance and found that decreased tunnel centre K^+ concentration improved discharge capacity and rate capability.[22] Second, Yoo *et al.* determined that transition metal ion doping of α-K_xMnO_2 with V and with Fe both lead to improvements in cyclability in LIBs, which were attributed to improved stability of the α-K_xMnO_2 phase due to the doped transition metal ions.

In this study we aimed to minimize the kinetic barriers to magnesiation and improve the stability of the α-K_xMnO_2 phase by framework doping of α-K_xMnO_2 with vanadium. V was chosen as the dopant due to its similar ionic radius to Mn and its higher valence (+5) compared to Mn (4+). Namely, we attempted the framework substitution of the higher valence V to stabilize the α-K_xMnO_2 phase, while simultaneously decreasing tunnel centre potassium occupancy due to the need to maintain charge neutrality.

2 Experimental

2.1 Preparation of vanadium doped α-K_xMnO_2

α-K_xMnO_2 with variable concentrations of doped vanadium was synthesized using a hydrothermal method reported by Polverejan *et al.*[25] 14.3 mmol $MnSO_4 \cdot 5H_2O$ (Nacalai Tesque, INC., Japan), 21.45 mmol K_2SO_4 (Nacalai Tesque, INC., Japan), and 21.45 mmol $K_2S_2O_8$ (FUJIFILM Wako Pure Chemical Co., Japan) were dissolved in 60 mL of deionized water. Vanadium was introduced by addition of Na_3VO_4 (MP Biomedicals, Inc., USA), and precursor concentration was controlled by using the V/(Mn + V) mole ratio. Four samples with ratios of 0, 5, 10, and 20 mol% were prepared. The solutions were each transferred to 100 mL PTFE (polytetrafluoroethylene)-lined stainless steel autoclaves and heated at 200 °C for 48 h. The obtained suspensions were filtered, washed three times with deionized water, and dried at 80 °C for 24 h to remove excess water. The obtained powders were ground and passed through a 150 μm mesh to minimize the impact of particle size on the electrochemical measurements. The expected synthesis reaction is:

$$MnSO_4 + K_2S_2O_8 + 2H_2O \rightarrow MnO_2 + K_2SO_4 + 2H_2SO_4,$$

Excess K_2SO_4 is used to provide K^+ ions used to stabilize the tunnel structure. The resulting solution is acidic due to the H_2SO_4 formed as a by-product of the synthesis reaction.

2.2 Materials characterization

Crystallographic characterization of the 4 obtained samples was performed by synchrotron X-ray diffraction (SXRD) at the BL02B2 beamline in SPring-8, using a 0.59999 Å incident beam, calibrated with a CeO_2 standard. X-ray photoelectron spectroscopy (XPS) measurements were carried out using an ULVAC-PHI

Quantera Instrument to analyse the valences of framework Mn and V. The morphologies and elemental distributions within the obtained powders were observed using a JEOL JSM-6010LA analytical scanning electron microscope with energy dispersive X-ray (EDX) analysis. Focused ion beam scanning electron microscopy (FIB-SEM) was performed using a Thermo fisher Scios 2 DualBeam microscope. Finally, bulk elemental compositions were analysed using an SPS 3500 series inductively coupled plasma (ICP) spectrometer.

2.3 Electrochemical measurements

All electrochemical tests were performed using a three-electrode beaker cell (Fig. S1†). The working electrode (WE) was composed of a slurry of the α-K_xMnO_2 active material, activated carbon conductive agent (Super P, Hohsen Co., Japan), and PVDF binder (KF polymer, Hohsen Co., Japan) at an 8 : 1 : 1 mass ratio, suspended in 600 μL of *N*-methyl-2-pyrrolidone (NMP, Nacalai Tesque, INC., Japan). The slurry was mixed using a rotation-revolution mixer (ARE-310, Thinky, Inc., Japan) at 2000 rpm for 20 min with an additional defoaming step at 2200 rpm for 2 min, before coating on a platinum current collector, and dried at 80 °C under vacuum for 24 h. The counter electrode (CE) was a 99.9% Mg ribbon, polished using #150 sandpaper under an Ar atmosphere. Finally, an Ag/Ag^+ reference electrode (RE) composed of an Ag wire immersed in 450 μL solution composed of 0.01 M $AgNO_3$, 0.1 M $Mg[TFSA]_2$, and (TFSA: bis(trifluoromethanesulfonyl)-amide) in triethylene glycol dimethyl ether (G3) in a glass tube with a porous Vycor® glass tip was employed. The electrolyte was prepared using a 10 mL volumetric flask by dissolving 0.5 mmol of magnesium bis(trifluoromethanesulfonamide) ($Mg[TFSA]_2$) (FUJIFILM Wako Pure Chemical Co., Japan) and 0.5 mmol tetraethyleneglycol dimethyl ether (G4) (FUJIFILM Wako Pure Chemical Co., Japan) in *N*-methyl-*N*-propylpyrrolidinium TFSA ([Pyr1,3][TFSA]) (FUJIFILM Wako Pure Chemical Co., Japan). This electrolyte will henceforth be denoted as 0.5 M $[Mg(G4)][TFSA]_2$/[Pyr1,3][TFSA].[26] The conversion from the Ag/Ag^+ reference potential to the Mg/Mg^{2+} potential was determined experimentally using the Mg deposition/dissolution potential for a Pt electrode at 100 °C as shown in Fig. S2.† The equation 0 V *vs.* $Mg/Mg^{2+} = -2.6$ V *vs.* Ag/Ag^+ was used to convert all recorded potentials. All electrochemical measurements were performed using a potentiostat (VSP-300, BioLogic, France).

3 Results and discussion

3.1 Chemical and structural characterization

The primary modifier examined in this study was the effect of V-doping of the α-K_xMnO_2 positive electrode active material on RMB performance. We analyzed the V and K contents for each of the obtained samples using ICP spectroscopy as tabulated in Table 1. The concentrations of doped V in the obtained powders were measured to be 4.3, 7.2, and 12.0 mol% for the 5, 10, and 20 mol% precursor mixtures, respectively.

Surprisingly, the concentration of potassium for each of the above four samples, measured by using K/(Mn + V) mole ratios, did not exhibit significant changes with values of 9.8, 12.8, 10.1, and 10.1 mol% respectively.

Table 1 Mole ratios of vanadium to manganese and potassium to manganese in obtained samples as analysed by using inductively coupled plasma (ICP) tabulated for each precursor ratio of vanadium and manganese

Precursor V/(Mn + V) mol%	Obtained V/(Mn + V) mol% (ICP)	Obtained K/(Mn + V) mol% (ICP)
0	0	9.8
5	4.3	12.8
10	7.2	10.1
20	12.0	10.1

Fig. 2a–d show the morphology and elemental mapping of V, Mn, and K measured for the 7.2% V-doped sample. We observe a homogeneous distribution of V, Mn, and K across the sample. Fig. 2e shows the SXRD peak profiles of the doped samples. Excluding slight contamination of the 4.3% V-doped sample with what appears to be $Mn_2V_2O_7$, the profiles exhibit characteristic peaks of α-K_xMnO_2. The presence of these characteristic peaks and the homogeneous distribution of V across the sample show that the added V doped the host α-K_xMnO_2, as opposed to forming separate V compounds. Additionally, we observed no significant shifts in peak position, and a slight broadening of peaks as the concentration of the dopant increases. At higher V concentrations crystallinity is decreased, as evidenced by the broadening of the peaks visible in the 12.0% V-doped sample. The samples with V concentrations greater than 12.0% were not considered for battery testing, due to the formation of separate V compounds during synthesis.

The location within the crystal lattice occupied by the doped V was analyzed by conducting four separate Rietveld refinements of the single SXRD profile for 7.2% V-doped α-K_xMnO_2 with the V position constrained to different Wyckoff positions within the α-K_xMnO_2 lattice. The 7.2% V-doped sample was chosen for this refinement due to the combination of high crystallinity and lack of visible contaminants as compared with the SXRD profiles for the other V-doped samples.

As described in detail in Fig. S3 and S4,† the Rietveld refinement with the V position constrained to the 8 h site illustrated improved fit to the SXRD peaks compared to the cases with other constrained positions. Despite there being no constraint on the location of the doped V beyond the Wyckoff position, the location of the doped V was only slightly offset from the location of the framework Mn. It is therefore likely that the doped-V mainly substituted the framework Mn. This result is reinforced by Raman spectroscopy measurements reported by Polverejan *et al.*[25] illustrating that only a single additional Raman peak, corresponding to the V–O single bond was present in the V-doped α-K_xMnO_2 samples.

XPS was employed to determine the averaged valence states of V and Mn. Fig. 3a compares the XPS profiles for the V $2p_{3/2}$ peaks of 7.2% V-doped α-K_xMnO_2 compared to a V_2O_5 reference. A charge reference of 284.8 eV was used for the measured

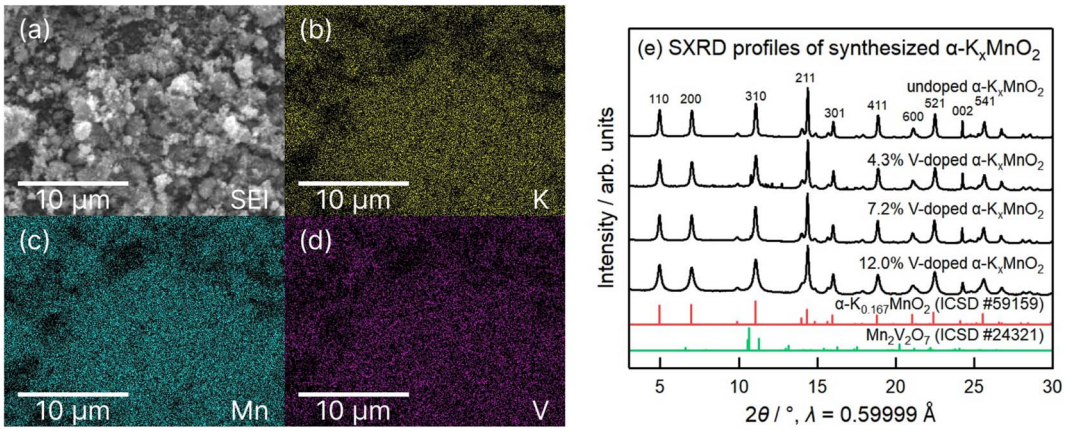

Fig. 2 (a) SEM image of 7.2% V-doped α-K_xMnO_2 and EDS elemental mapping of the corresponding area for (b) potassium, (c) manganese, and (d) vanadium. (e) SXRD profiles of undoped, 4.3% V-doped, 7.2% V-doped, and 12.0% V-doped α-K_xMnO_2.

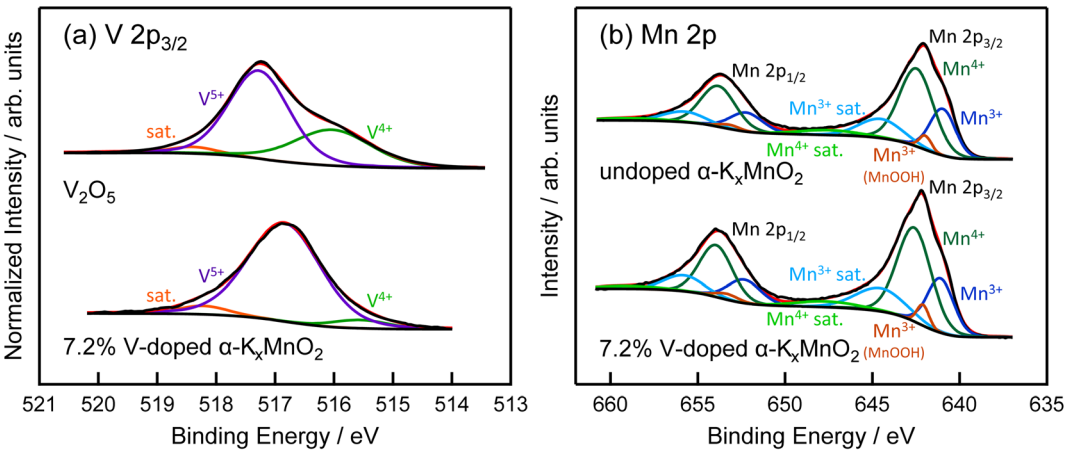

Fig. 3 X-ray photoelectron spectra: (a) V 2$p_{3/2}$ peak of V_2O_5 and 7.2% V-doped α-K_xMnO_2 and (b) Mn 2p peaks of undoped α-K_xMnO_2 and 7.2% V-doped α-K_xMnO_2.

adventitious C 1s peaks. The V 2$p_{1/2}$ peak was not considered for this fitting due to the partial overlap with the O 1s peak. It was concluded that the valence of the doped V was most likely +5. A slight difference in the binding energies of the V^{5+} peaks of V_2O_5 and V-doped α-K_xMnO_2 is generally expected due to the differences in the bonding environments of the two samples.[27] The satellite (sat.) peaks are thought to be related to surface adsorption.

The average valence of Mn was analyzed by fitting of Mn 2p peak profiles measured by XPS for undoped and 7.2% V-doped α-K_xMnO_2, respectively, as shown in Fig. 3b. The average Mn valence for each sample, calculated using the ratio of Mn^{3+} and Mn^{4+} peak area, was roughly +3.6. Detailed area ratios are provided in Table S2.† This result is corroborated by the good fit of the O 1s lattice oxygen peaks, provided in Fig. S5 and Table S3,† when constrained by the area ratios in accordance with the Mn^{3+} and Mn^{4+} ratios calculated in the above Mn 2p profiles. The addition of V^{5+} without change in the average Mn valence necessitates a change in either oxygen vacancy concentration, or tunnel cation concentration to maintain charge neutrality of the synthesized sample. These mechanisms and the effects on RMB performance will be discussed in greater detail in Section 3.5.

3.2 Constant current discharge–charge analysis

We evaluated the discharge performance of the RMBs with undoped and V-doped α-K_xMnO_2 positive electrode active materials to determine the effect of V-doping on the discharge potential and initial discharge capacity. The four α-K_xMnO_2 variants were tested at 100 °C using a constant discharge current density of 10 mA g^{-1}, with a capacity cutoff of 200 mA h g^{-1}. The capacity cutoff of 200 mA h g^{-1} was implemented as α-MnO_2 had been shown to exhibit irreversible conversion to rock-salt phase MgO–MnO at capacities exceeding 220 mA h g^{-1}.[16]

The discharge profiles for the four α-K_xMnO_2 samples are shown in Fig. 4a. The first point of interest is the 0.2 V – 0.3 V increase in initial discharge potential seen in every V-doped α-K_xMnO_2 sample compared to the undoped α-K_xMnO_2. This increased discharge potential is ascribed to a decrease in overpotential for the Mn^{4+}/Mn^{3+} reduction reaction as opposed to

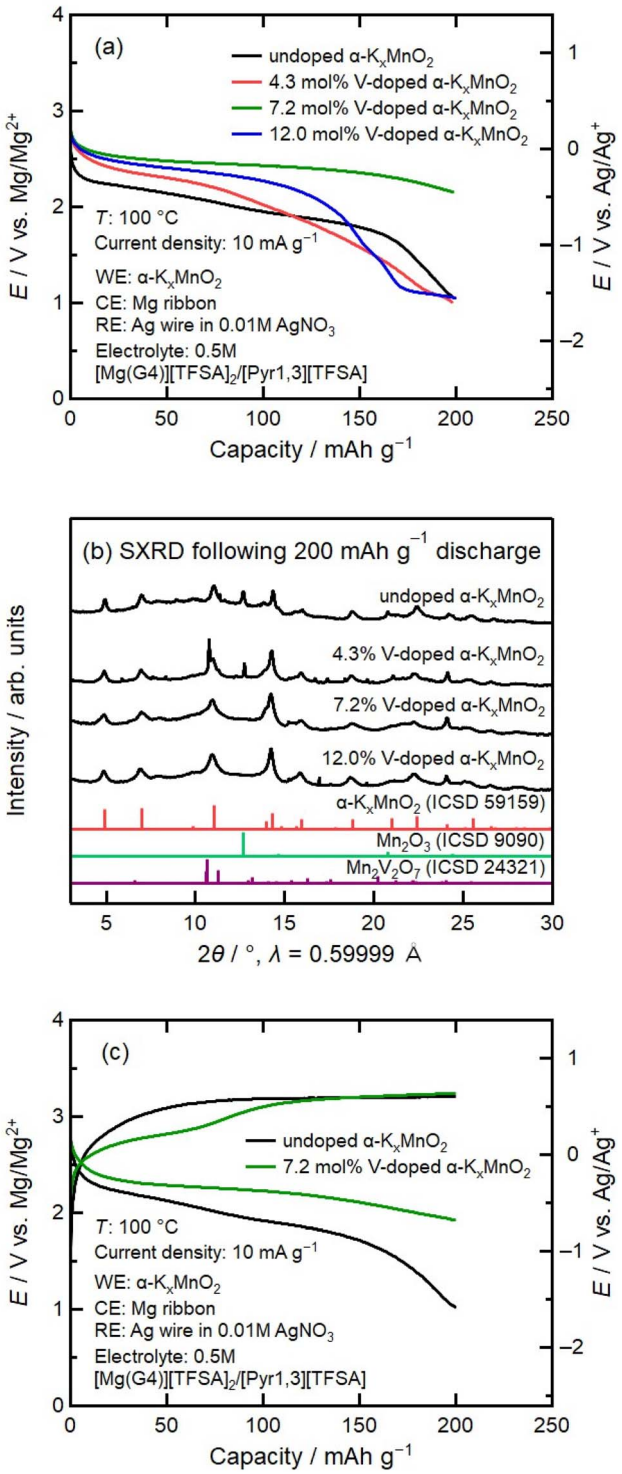

Fig. 4 (a) Constant current discharge curves of undoped and V-doped α-K_xMnO_2, (b) SXRD profiles of undoped and V-doped α-K_xMnO_2 following constant current discharge to 200 mA h g^{-1} shown in (a). (c) Constant current discharge–charge curves of undoped and 7.2% V-doped α-K_xMnO_2.

a separate V^{5+}/V^{4+} redox reaction, as the theoretical discharge capacity for the V^{5+}/V^{4+} redox couple is limited to 12.7, 21.3, and 35.6 mA h g^{-1} for the 4.3%, 7.2% and 12.0% V-doped α-K_xMnO_2, respectively.

Secondly, there is a retention of higher discharge potentials in the case of the 7.2% V-doped sample, as the discharge potential exceeds 2 V *vs.* Mg/Mg^{2+} at the 200 mA h g^{-1} cutoff. In contrast, all other samples experienced significant declines in discharge potential before the capacity cutoff. The SXRD profiles of the four samples following discharge are provided in Fig. 4b. In the undoped and 4.3% V-doped samples, we observe an additional Mn_2O_3 peak that is not present in the 7.3% and 12.0% V-doped samples. The presence of Mn_2O_3 peaks in addition to the α-K_xMnO_2 peaks shows that some portion of reduction during discharge progressed by conversion of the framework α-K_xMnO_2 as opposed to reduction accompanied by Mg^{2+} insertion. The lack of visible Mn_2O_3 peaks in the 7.2% and 12.0% V-doped samples suggest that the presence of the V within the α-K_xMnO_2 lattice limits the favorability of the conversion mechanism.

Given the improved performance of the 7.2% V-doped sample, we further investigated 7.2% V-doped α-K_xMnO_2 in detail.

Fig. 4c compares the discharge–charge profiles of 7.2% V-doped and undoped α-K_xMnO_2. The 7.2% V-doped sample exhibits a charge plateau at about 2.8 V *vs.* Mg/Mg^{2+} that is not observed in the undoped sample. Elemental composition of post discharge and post discharge–charge samples for both undoped α-K_xMnO_2 and 7.2% V-doped α-K_xMnO_2 was analyzed using ICP spectroscopy. The analyzed magnesium content for each sample is provided in Table 2. V-doping increases the Mg concentration after discharge and enables greater Mg extraction after subsequent charging. This greater magnitude of insertion and extraction indicates that V-doping improves Mg^{2+} mobility within the host framework both for discharge and charge processes. Additionally, there is no decrease in V concentration in the 7.2% V-doped α-K_xMnO_2 across the charge cycle. Therefore, the oxidative reaction observed at 2.8 V *vs.* Mg/Mg^{2+} is likely caused by the extraction of magnesium from the host framework, and not by extraction or dissolution of the doped V. Another point to consider is the lower total concentration of magnesium compared to theoretical values. This implies the presence of background electrolyte decomposition, the contribution of other cations such as protons, or potential dissolution of magnesium-based conversion products, all leading to lower-than-expected values of detected magnesium.[28]

3.3 Effect of V-doping on redox pathways

To better determine the effect of V-doping of α-K_xMnO_2 on the reduction and oxidation mechanisms, we performed cyclic voltammetry (CV) starting at the open circuit potential with 1 V *vs.* Mg/Mg^{2+} and 3.6 V *vs.* Mg/Mg^{2+} as the lower and upper bounds, respectively. The voltammograms of undoped and 7.2% V-doped α-K_xMnO_2 are presented in Fig. 5. All voltammetry measurements were performed at 100 °C to match the conditions of the discharge–charge tests.

The two separate cathodic peaks at 2.1 V *vs.* Mg/Mg^{2+} and 1.7 V *vs.* Mg/Mg^{2+} seen in each scan illustrate the presence of two separate reduction reactions. The V-doped sample exhibits higher current densities for the 2.1 V *vs.* Mg/Mg^{2+} peak

Table 2 Ratio of Mg to framework Mn and V for undoped and 7.2% V-doped α-K_xMnO_2 estimated by ICP spectroscopy after galvanostatic discharge to 200 mA h g^{-1} and after galvanostatic discharge followed by charge to 200 mA h g^{-1}

Sample description	Experimental condition	Theoretical Mg/(Mn + V) calc. from electrochemical capacity (mol%)	Experimental Mg/(Mn + V) estimated by using ICP (mol%)	Experimental V/(Mn + V) in powder samples estimated by using ICP (mol%)	Experimental V/(Mn + V) estimated by using ICP (mol%)
Undoped α-K_xMnO_2	Discharge to 200 mA h g^{-1}	33.9	1.23 (3.6%)	0	0
	Charge to 200 mA h g^{-1} following discharge	0	0	0	0
7.2% V-doped α-K_xMnO_2	Discharge to 200 mA h g^{-1}	33.9	5.66 (16.7%)	7.2	7.2
	Charge to 200 mA h g^{-1} following discharge	0	0.65	7.2	8.1

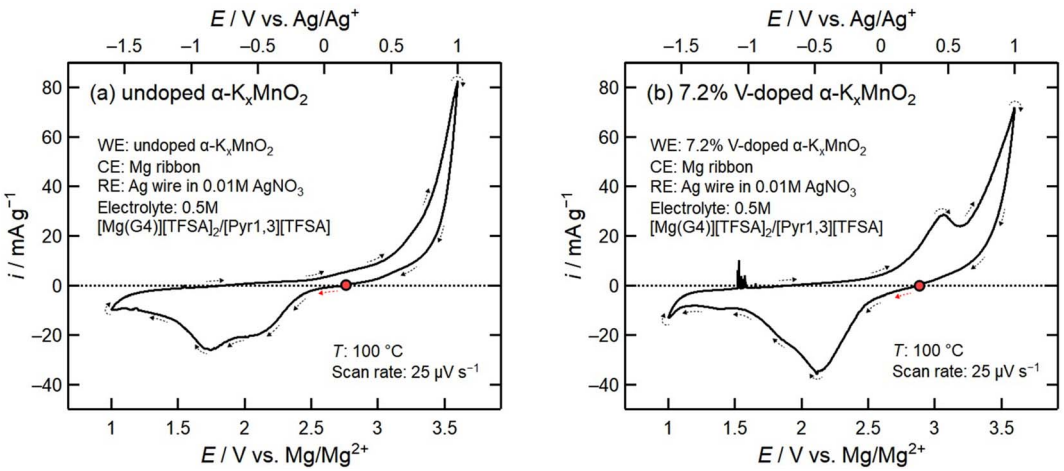

Fig. 5 (a) Cyclic voltammogram of undoped α-K_xMnO_2 measured at a scan rate of 25 μV s^{-1} at 100 °C. (b) Cyclic voltammogram of 7.2% V-doped α-K_xMnO_2 measured at a scan rate of 25 μV s^{-1} at 100 °C.

compared to the undoped sample, and significantly lower current densities for the 1.7 V *vs.* Mg/Mg^{2+} redox peak, which agrees well with the discharge curves shown in Fig. 4a. V-doping improves the selectivity of the redox reaction with the higher potential, while suppressing the reaction at 1.7 V *vs.* Mg/Mg^{2+}.

In the anodic scan, the voltammogram of 7.2% V-doped α-K_xMnO_2 shows a significant anodic peak at 3.1 V *vs.* Mg/Mg^{2+} which is not present in the undoped α-K_xMnO_2 profile, indicating a separate oxidation reaction. In both voltammograms there is an increase in anodic current starting above 3 V *vs.* Mg/Mg^{2+} up to the upper potential limit of 3.6 V *vs.* Mg/Mg^{2+}. We believe this anodic current to be caused by oxidative electrolyte decomposition as the magnitude and onset potentials align with previously reported values for oxidative electrolyte decomposition of the $[Mg(G4)][TFSA]_2$/[Pyr1,3][TFSA] electrolyte.[12,29]

To investigate the reduction mechanisms for the two separate cathodic peaks at 2.1 V *vs.* Mg/Mg^{2+} and 1.7 V *vs.* Mg/Mg^{2+}, we performed two additional linear sweep voltammetry (LSV) experiments from OCP to 2 V *vs.* Mg/Mg^{2+} and OCP to 1 V *vs.* Mg/Mg^{2+} for undoped α-K_xMnO_2. Fig. 6a compares the two LSV profiles, and Fig. 6b compares the two SXRD profiles corresponding to the samples following each experiment. The SXRD profile following the potential sweep from OCP to 2.1 V *vs.* Mg/Mg^{2+} shows characteristic α-K_xMnO_2 peaks without obvious impurity peaks. In contrast, we see the presence of many new peaks in addition to the α-K_xMnO_2 peaks following a cathodic potential sweep to 1 V *vs.* Mg/Mg^{2+}. Notably there are several peaks corresponding to Mn_3O_4, but no Mn_2O_3 peaks as previously observed in the discharged samples, possibly due to further conversion of Mn_2O_3 to Mn_3O_4. In addition, there were several peaks that could not be identified, likely caused by distortion of the α-K_xMnO_2 tunnels upon high levels of magnesiation. These SXRD profiles indicate that the redox reaction at 2.1 V *vs.* Mg/Mg^{2+} corresponds to reduction of α-K_xMnO_2 *via* magnesiation, while the 1.7 V *vs.* Mg/Mg^{2+} redox reaction is a conversion from α-K_xMnO_2 to different Mg–Mn oxide phases. The significant increase in the 2.1 V *vs.* Mg/Mg^{2+} cathodic peak in the 7.2% V-doped cyclic voltammogram in Fig. 5b therefore correlates with improved magnesium mobility, while the significantly smaller peak at 1.7 V *vs.* Mg/Mg^{2+} shows that the addition of vanadium limited the progression of the conversion reaction by improving the stability of the α-K_xMnO_2 phase.

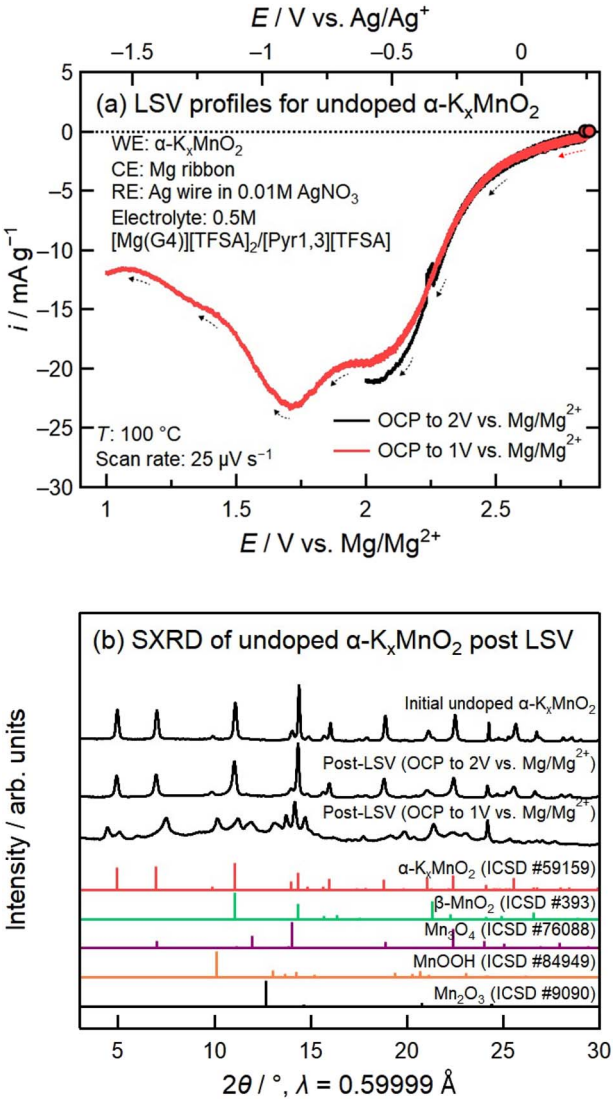

Fig. 6 (a) Linear sweep voltammograms of undoped α-K_xMnO_2 from OCP to 2 V *vs.* Mg/Mg^{2+} and OCP to 1 V *vs.* Mg/Mg^{2+}. (b) SXRD profiles of undoped α-K_xMnO_2 as-synthesized powder and composite electrodes containing undoped α-K_xMnO_2 following LSV from OCP to 2 V *vs.* Mg/Mg^{2+} and OCP to 1 V *vs.* Mg/Mg^{2+}.

3.4 Effect of V-doping on RMB cyclability

The effect of V-doping on the cyclability of α-K_xMnO_2 was examined using galvanostatic cycling with potential limitation (GCPL) across ten discharge–charge cycles. Undoped and 7.2% V-doped α-K_xMnO_2 samples were evaluated at a constant current density of 10 mA g^{-1} with potential cutoffs of 2 V and 3.6 V *vs.* Mg/Mg^{2+}. The 2 V *vs.* Mg/Mg^{2+} cutoff was set for two reasons. Firstly, the cutoff at 2 V *vs.* Mg/Mg^{2+} prevents discharge by the conversion mechanism. As shown in Section 3.3, discharge progresses by Mg^{2+} insertion at potentials above 2 V *vs.* Mg/Mg^{2+}, but switches to a conversion mechanism at lower potentials. Secondly, the cutoff prevents reductive electrolyte decomposition upon discharge, as the onset of reductive electrolyte decomposition is not expected above 2 V *vs.* Mg/Mg^{2+}.

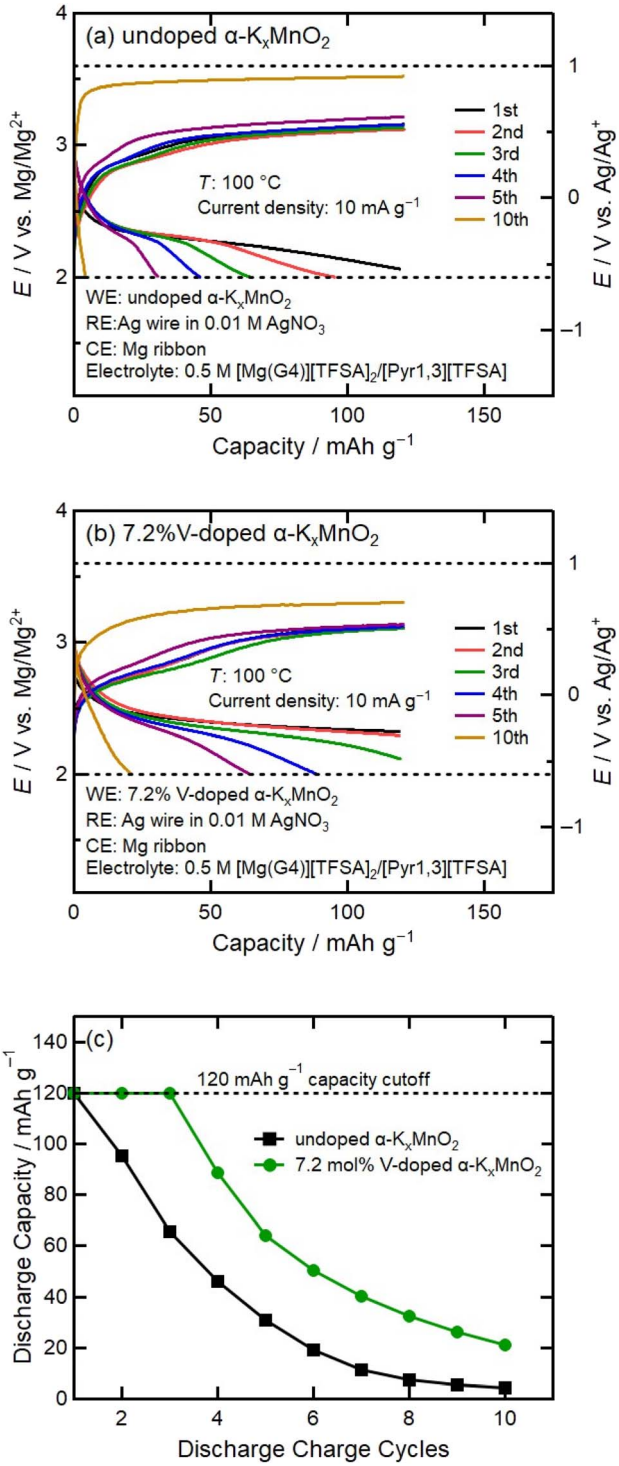

Fig. 7 (a) Galvanostatic cycling with potential limitation (GCPL) profile for undoped α-K_xMnO_2 measured at a current density of 10 mA g^{-1} and 2 V and 3.6 V *vs.* Mg/Mg^{2+} potential cutoffs. (b) GCPL profile for 7.2% V-doped α-K_xMnO_2 measured at a current density of 10 mA g^{-1} and 2 V and 3.6 V *vs.* Mg/Mg^{2+} potential cutoffs. (c) Discharge capacity plotted against cycle number for undoped and 7.2% V-doped α-K_xMnO_2.

Fig. 7a and b plot the discharge potentials for undoped α-K_xMnO_2 and 7.2% V-doped α-K_xMnO_2, respectively across the ten cycles. There is a clear decrease in capacity during cycling in both samples; however, the magnitude of this decrease is suppressed in the V-doped sample as shown in Fig. 7c. This improvement in cyclability caused by V-doping alone is promising, as there remain many factors that can be modified to further increase cyclability. Investigation into the effects of different cation species within the tunnel centre, co-insertion of Mg^{2+} as part of a chelated complex or other electrolyte additives and multiple possible framework dopants provide many options for further improvements.

3.5 Screening of mechanisms for improved RMB performance

We have thus far shown how V-doping of α-K_xMnO_2 leads to greater Mg^{2+} mobility, as evidenced by the greater current densities corresponding to Mg^{2+} insertion and extraction, and greater phase stability. Here we posit that the presence of V^{5+} can explain the improved stability, while a decrease in H^+ occupying the α-K_xMnO_2 tunnel in the V-doped sample is responsible for the increase in Mg^{2+} mobility.

Several factors were considered as explanations for the increased mobility and stability. We considered a decrease in oxygen vacancy concentration, effects of V–O bonding, a decrease in grain size, an increase in tunnel diameter, and a decrease in cation concentrations within the tunnel structure in the V-doped sample as possible explanations. Each factor above was considered as they can offer explanations for the observed improvement in the Mg^{2+} mobility or α-K_xMnO_2 phase stability.

An increase in oxygen vacancy concentration has been shown across multiple studies to decrease the stability of transition metal oxide active materials in LIBs, causing cracking and dissolution of the transition metal ions.[30,31] The concentrations of oxygen vacancies in both samples were calculated using the ratio of atomic concentrations of Mn, V and O obtained *via* XPS. There was no appreciable difference in atomic concentration of O across the two samples, with atomic percentages of 63.7% and 63.0% for the undoped and 7.2% V-doped samples, respectively (Table S4†). Combined with the minimal difference in the ratio of lattice and absorbed oxygen peak areas of 67.7% for undoped α-K_xMnO_2 and 68.8% for 7.2% V-doped α-K_xMnO_2 detailed in Table S3,† it can be concluded that there is minimal change in oxygen vacancy concentration caused by V-doping, and that changes in oxygen vacancy concentration are unlikely to be the explanation for the improved phase stability. Consequently, we considered differences between the framework Mn and doped V that could explain the improved stability. Differences in the valence, ionic size, and M–O bond distance of the doped V from those of the framework Mn may offer explanations. Density functional theory (DFT) calculations of transition metal dopants in LIBs by Brady *et al.* showed that transition metal dopants such as Nb^{5+} may be able to suppress tunnel breakage at high degrees of lithiation.[21] In particular, they reported that these dopants improve the stability of the α-MnO_2 phase during lithiation by preventing the breakage of bonds within the framework MO_6 octahedra. While we believe a similar comprehensive review of transition metal dopants of α-MnO_2 for RMBs is required to fully elucidate the mechanism, the greater difference in charge of the V^{5+}–O^{2-} bond compared to the $Mn^{3.6+}$–O^{2-} bond could be responsible for a similar suppression of tunnel breakage.

A smaller average grain size caused by V-doping was investigated as a possible explanation for the improved Mg^{2+} mobility. A smaller grain size has been shown to correlate with improved battery performance in RMBs.[32,33] As the size of the grain decreases, the ratio of surface area to volume increases. In their study on α-MnO_2 active materials in RMBs, Ling *et al.* showed that Mg^{2+} insertion upon discharge was often limited to the exterior surface of the α-MnO_2 particle due to the sluggish diffusion of Mg^{2+}.[14] As such we considered that a smaller grain size could explain the observed increase in current density. The grain size of the undoped and 7.2% V-doped samples was compared using high-resolution SEM as shown in Fig. 8a and b. Both samples exhibit similar morphologies, composed of numerous capsule-shaped grains, with dimensions of approximately 50 nm × 100 nm. The cross-section images of the two samples (Fig. S6†) also show similar clustering of these small grains. As such, we concluded that there is no appreciable change in grain size due to V-doping, and that a decrease in grain size due to V-doping is not likely to be the mechanism by which RMB performance is improved.

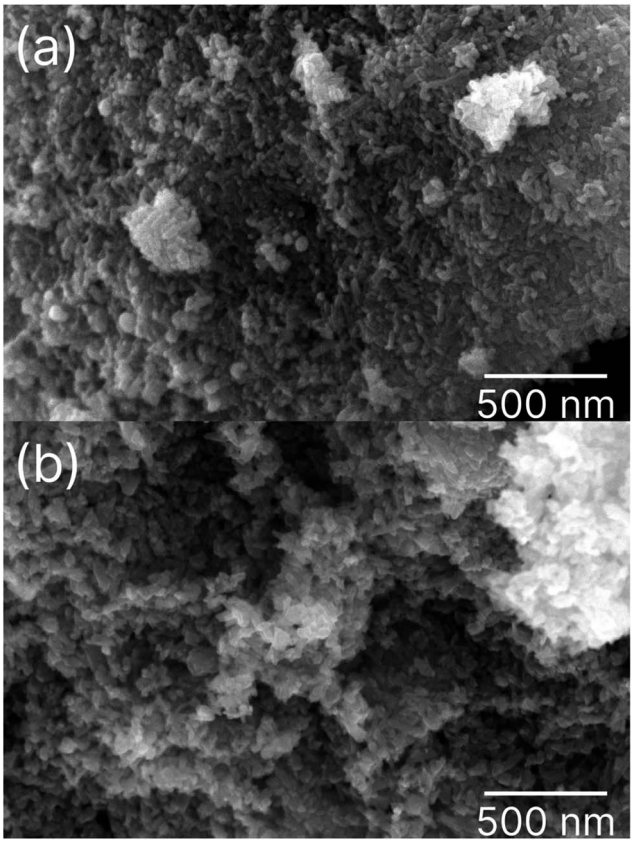

Fig. 8 High-resolution SEM images of (a) undoped α-K_xMnO_2 and (b) 7.2% V-doped α-K_xMnO_2.

Second, we posited an increase in tunnel diameter due to V-doping as a mechanism for improved Mg^{2+} mobility. It is expected that a greater tunnel diameter would result in lower electrostatic interaction. Similar methods have been employed to great success in layered oxides with larger interlayer spacing leading to improved Mg^{2+} kinetics.[34–37] The horizontal lattice constant *a* was considered as it is proportional to the tunnel diameter. The lattice constants for both samples, calculated *via* Rietveld refinement are equivalent, with calculated values of 9.839 Å and 9.842 Å for undoped and 7.2% V-doped α-K_xMnO_2, respectively. We concluded that the tunnel size is not affected by V-doping, and that modified tunnel size is not the mechanism by which RMB performance was improved.

Lastly, a change in the concentration of cations within the α-MnO_2 tunnel structure is considered. A decrease in tunnel centre cation concentration may decrease the electrostatic repulsion with the inserted Mg^{2+} ions. Proyaz *et al.* previously showed that a smaller K^+ concentration in α-K_xMnO_2 improved performance in LIBs.[22] As previously discussed in Section 3.1, ICP analysis of K/(Mn + V) molar ratios shows equivalent concentrations of tunnel centre K^+ across all samples. A change in K^+ concentration therefore cannot explain the improved performance. However, the α-K_xMnO_2 tunnel may contain molecules other than K^+, as both H_2O and H^+ may be introduced during the hydrothermal synthesis. Both H_2O and H^+ are capable of occupying the tunnel complex of α-MnO_2, as shown by Dai *et al.*[38] and Johnson *et al.*[39] A decrease in H^+ concentration from the undoped to the 7.2% V-doped sample provides an explanation for the mechanism by which charge neutrality is maintained in the V-doped sample, with a decrease in H^+ concentration accompanying the substitution of $Mn^{3.6+}$ with V^{5+}. The decrease in H^+ concentration would consequently decrease the electrostatic repulsion experienced by the Mg^{2+} during insertion and extraction, as there would be fewer cationic species within the tunnel to obstruct the Mg^{2+} diffusion. Further investigation is needed to isolate the impact of tunnel centre H^+ in α-MnO_2 active materials on RMBs.

4 Conclusions

In conclusion, doping of α-K_xMnO_2 with V ions was carried out to observe the effects of the introduction of higher valence transition metal ions on RMB performance. We successfully doped α-K_xMnO_2 with three different concentrations of vanadium *via* a hydrothermal process. Successful doping was characterized by the even distribution of V within the host α-K_xMnO_2 and Rietveld refinement of the SXRD profiles. We showed that V-doping took place *via* substitution of V for framework Mn. The substituted V had a valence of +5, while the Mn valence did not change due to V-doping with an average valence of +3.6 in both the undoped and V-doped samples.

Furthermore, the effect of this V-doping on α-K_xMnO_2 positive electrode performance in RMBs was evaluated. We determined that V-doping leads to an increase in initial RMB discharge potential by 0.2 V to 0.3 V compared to that of undoped α-K_xMnO_2. Additionally, we determined that at limited concentrations such as 7.2% V, the addition of V stabilized the α-K_xMnO_2 framework, leading to a greater degree of reduction with Mg^{2+} insertion, and a significant decrease in reduction accompanied by conversion of α-K_xMnO_2 to disparate Mn oxide phases.

We also observed that V-doping improved the mobility of Mg^{2+} ions during oxidation, resulting in a significant increase in Mg^{2+} extraction observed in both cyclic voltammograms and constant current charge profiles. This improved Mg^{2+} mobility allowed for an improvement in RMB cyclability.

We investigated possible mechanisms to explain the greater Mg^{2+} mobility and α-K_xMnO_2 stability in the V-doped sample. We posited that changes in the concentration of H^+ occupying the α-K_xMnO_2 tunnel could be responsible for the improved Mg^{2+} insertion kinetics, while a greater difference in charge of the V–O bond compared to the Mn–O bond could be responsible for the improved stability. We also ruled out the possibility of changes in grain size, tunnel dimensions, and oxygen vacancy concentrations as explanations for the observed improvements.

The significant improvement in the RMB performance of V-doped α-K_xMnO_2 paves the way for further improvements to achieve RMB practical applications by way of transition metal doping.

Author contributions

Isaac Oda-Bayliss: investigation, writing – original draft, writing – review & editing. Shunsuke Yagi: supervision, writing – review & editing, funding acquisition. Masao Kamiko: resources, validation. Kai Shimada: investigation. Hiroaki Kobayashi: discussion. Tetsu Ichitsubo: supervision.

Conflicts of interest

There are no conflicts to declare.

Acknowledgements

This study was supported by the GteX Program Japan Grant Number JPMJGX23S1 and the Japan Society for the Promotion of Science (JSPS: 23H05452). SXRD measurements were conducted at the BL02B2 beamline (Proposal No. 2023A1728 and 2023B1635) at SPring-8. The data shown in Fig. 8a and b were observed at Komaba Analysis Core, Institute of Industrial Science, The University of Tokyo, and data analysis was supported by Dr Atsushi Fukuda. The authors acknowledge their support.

References

1 J. M. Tarascon and M. Armand, *Nature*, 2001, **414**, 359–367.
2 S. Yagi, A. Tanaka, T. Ichitsubo and E. Matsubara, *ECS Electrochem. Lett.*, 2012, **1**, D11–D14.
3 M. Matsui, *J. Power Sources*, 2011, **196**, 7048–7055.
4 M. Morita, N. Yoshimoto, S. Yakushiji and M. Ishikawa, *Electrochem. Solid-State Lett.*, 2001, **4**, A177–A179.

5 S. Yagi, A. Tanaka, Y. Ichikawa, T. Ichitsubo and E. Matsubara, *J. Electrochem. Soc.*, 2013, **160**, C83–C88.
6 S. Yagi, A. Tanaka, Y. Ichikawa, T. Ichitsubo and E. Matsubara, *Res. Chem. Intermed.*, 2014, **40**, 3–9.
7 D. Aurbach, Z. Lu, A. Schechter, Y. Gofer, H. Gizbar, R. Turgeman, Y. Cohen, M. Moshkovich and E. Levi, *Nature*, 2000, **407**, 724–727.
8 Y. Nuli, Y. Zheng, Y. Wang, J. Yang and J. Wang, *J. Mater. Chem.*, 2011, **21**, 12437–12443.
9 T. Hatakeyama, N. L. Okamoto, K. Shimokawa, H. Li, A. Nakao, Y. Uchimoto, H. Tanimura, T. Kawaguchi and T. Ichitsubo, *Phys. Chem. Chem. Phys.*, 2019, **21**, 23749–23757.
10 S. Okamoto, T. Ichitsubo, T. Kawaguchi, Y. Kumagai, F. Oba, S. Yagi, K. Shimokawa, N. Goto, T. Doi and E. Matsubara, *Adv. Sci.*, 2015, **2**, 1500072.
11 J. Han, S. Yagi and T. Ichitsubo, *J. Power Sources*, 2019, **435**, 226822.
12 J. Han, S. Yagi, H. Takeuchi, M. Nakayama and T. Ichitsubo, *J. Mater. Chem. A*, 2021, **9**, 26401–26409.
13 R. Zhang, X. Yu, K. W. Nam, C. Ling, T. S. Arthur, W. Song, A. M. Knapp, S. N. Ehrlich, X. Q. Yang and M. Matsui, *Electrochem. Commun.*, 2012, **23**, 110–113.
14 C. Ling, R. Zhang, T. S. Arthur and F. Mizuno, *Chem. Mater.*, 2015, **27**, 5799–5807.
15 T. S. Arthur, R. Zhang, C. Ling, P. A. Glans, X. Fan, J. Guo and F. Mizuno, *ACS Appl. Mater. Interfaces*, 2014, **6**, 7004–7008.
16 T. Hatakeyama, H. Li, N. L. Okamoto, K. Shimokawa, T. Kawaguchi, H. Tanimura, S. Imashuku, M. Fichtner and T. Ichitsubo, *Chem. Mater.*, 2021, **33**, 6983–6996.
17 H. N. Yoo, D. H. Park and S. J. Hwang, *J. Power Sources*, 2008, **185**, 1374–1379.
18 A. M. Hashem, H. M. Abuzeid, D. Mikhailova, H. Ehrenberg, A. Mauger and C. M. Julien, *J. Mater. Sci.*, 2012, **47**, 2479–2485.
19 J. G. Radich, Y.-S. Chen and P. V. Kamat, *ECS J. Solid State Sci. Technol.*, 2013, **2**, M3178–M3181.
20 T. Sasaki, S. Komaba, N. Kumagai and I. Nakai, *Electrochem. Solid-State Lett.*, 2005, **8**, A471.
21 A. B. Brady, K. R. Tallman, E. S. Takeuchi, A. C. Marschilok, K. J. Takeuchi and P. Liu, *J. Phys. Chem. C*, 2019, **123**, 25042–25051.
22 A. S. Poyraz, J. Huang, C. J. Pelliccione, X. Tong, S. Cheng, L. Wu, Y. Zhu, A. C. Marschilok, K. J. Takeuchi and E. S. Takeuchi, *J. Mater. Chem. A*, 2017, **5**, 16914–16928.
23 L. M. Housel, L. Wang, A. Abraham, J. Huang, G. D. Renderos, C. D. Quilty, A. B. Brady, A. C. Marschilok, K. J. Takeuchi and E. S. Takeuchi, *Acc. Chem. Res.*, 2018, **51**, 575–582.
24 M. M. Thackeray, *Prog. Solid State Chem.*, 1997, **25**, 1–71.
25 M. Polverejan, J. C. Villegas and S. L. Suib, *J. Am. Chem. Soc.*, 2004, **126**, 7774–7775.
26 T. Mandai, K. Tatesaka, K. Soh, H. Masu, A. Choudhary, Y. Tateyama, R. Ise, H. Imai, T. Takeguchi and K. Kanamura, *Phys. Chem. Chem. Phys.*, 2019, **21**, 12100–12111.
27 J. F. Watts and J. Wolstenholme, *The Electron Spectrum: Qualitative and Quantitative Interpretation*, Wiley, 2003.
28 X. Ye, H. Li, T. Hatakeyama, H. Kobayashi, T. Mandai, N. L. Okamoto and T. Ichitsubo, *ACS Appl. Mater. Interfaces*, 2022, **14**, 56685–56696.
29 J. Han, S. Yagi, H. Takeuchi, M. Nakayama and T. Ichitsubo, *J. Phys. Chem. C*, 2022, **126**, 19074–19083.
30 Q. Li, D. Ning, D. Wong, K. An, Y. Tang, D. Zhou, G. Schuck, Z. Chen, N. Zhang and X. Liu, *Nat. Commun.*, 2022, **13**, 1123.
31 Z. K. Tang, Y. F. Xue, G. Teobaldi and L. M. Liu, *Nanoscale Horiz.*, 2020, **5**, 1453–1466.
32 W. Chen, X. Zhan, B. Luo, Z. Ou, P. C. Shih, L. Yao, S. Pidaparthy, A. Patra, H. An, P. V. Braun, R. M. Stephens, H. Yang, J. M. Zuo and Q. Chen, *Nano Lett.*, 2019, **19**, 4712–4720.
33 L. Li, G. Hu, Y. Cao, D. Gong, Q. Fu, Z. Peng and K. Du, *Electrochim. Acta*, 2022, **435**, 141386.
34 Y. Li, Y. Zheng, K. Guo, J. Zhao and C. Li, *Energy Mater. Adv.*, 2022, **2022**, 9840837.
35 J. Tian, X. Zhou, Q. Wu and C. Li, *Energy Storage Mater.*, 2019, **22**, 218–227.
36 Z. Yao, Y. Yu, Q. Wu, M. Cui, X. Zhou, J. Liu and C. Li, *Small*, 2021, **17**, 2102168.
37 M. Wang and S. Yagi, *J. Alloys Compd.*, 2020, **820**, 153135.
38 J. Dai, S. F. Li, K. Siong Siow and Z. Gao, *Electrochim. Acta*, 2000, **45**, 2211–2217.
39 C. S. Johnson, D. W. Dees, M. F. Mansuetto, M. M. Thackeray, D. R. Vissers, D. Argyriou, C.-K. Loong and L. Christensen, *J. Power Sources*, 1997, **68**, 570–577.